### PHYSICAL REVIEW D 94, 044049 (2016)

# Initial-data contribution to the error budget of gravitational waves from neutron-star binaries

Antonios Tsokaros, <sup>1</sup> Bruno C. Mundim, <sup>1</sup> Filippo Galeazzi, <sup>1</sup> Luciano Rezzolla, <sup>1,2</sup> and Kōji Uryū<sup>3</sup>

<sup>1</sup>Institute for Theoretical Physics, Max-von-Laue-Straße 1, 60438 Frankfurt am Main, Germany

<sup>2</sup>Frankfurt Institute for Advanced Studies, Ruth-Moufang-Straße 1, D-60438 Frankfurt am Main, Germany

<sup>3</sup>Department of Physics, University of the Ryukyus, Senbaru, Nishihara, Okinawa 903-0213, Japan

(Received 23 May 2016; published 25 August 2016)

As numerical calculations of inspiraling neutron-star binaries reach values of accuracy that are comparable with those of black-hole binaries, a fine budgeting of the various sources of error becomes increasingly important. Among such sources, the initial data are normally not accounted for, the rationale being that the error on the initial spacelike hypersurface is always far smaller than the error gained during the evolution. We here consider critically this assumption and perform a comparative analysis of the gravitational waveforms relative to essentially the same physical binary configuration when computed with two different initial-data codes, and then evolved with the same evolution code. More specifically, we consider the evolution of irrotational neutron-star binaries computed either with the pseudospectral code LORENE, or with the newly developed finite-difference code COCAL; both sets of initial data are subsequently evolved with the high-order-evolution code WHISKYTHC. In this way we find that although global quantities of the system, like the mass and angular momentum, have differences of the order of ≤0.02%, local quantities, like rest-mass density, extrinsic curvature or angular velocity, show pointwise differences that are much larger, of the order of ≤1%. These local differences are then responsible for a dephasing in the gravitational waves at the merger time (after approximately three orbits) of  $\sim 1.4$  radians. Our results highlight the importance of using initial data that are pointwisely the same when comparative studies are done and physical parameters are estimated.

### DOI: 10.1103/PhysRevD.94.044049

### I. INTRODUCTION

With the first direct detection of gravitational waves from a merging system of black holes [1], the long-awaited gravitational-wave astronomy has finally become a reality in which a series of advanced interferometers such as LIGO, GEO, Virgo, KAGRA, and ET [2–6] is eagerly operating to unveil that part of the Universe that can be observed in terms of gravitational radiation. Neutron-star binary systems are prime actors of this Universe and have received enormous attention over the last ten years.

In addition, neutron-star binaries are leading candidates for the engine of short gamma-ray bursts [7–11] and possible sites for the production of the heaviest elements in the Universe [12–21]. Starting from the first successful simulations of binary neutron-star mergers [22] and the first complete description of this process from the inspiral down to the formation of an accreting black-hole–torus system [23], considerable progress has been made, so that it is now possible to consider rather realistic scenarios involving nuclear physics equations of state [24,25], neutrino cooling [18,19,26,27] and magnetohydrodynamics [28–32].

Obviously, any simulation of neutron-star binaries needs initial data to get started, and this is carefully crafted through standalone codes like COCAL [33,34], LORENE [35], KADATH [36], and SCRID [37,38], or through the elliptic solvers of evolution codes like SPEC [39], Princeton's [40],

or BAM [41]. Although the first initial data for neutron-star binaries have been computed for corotating systems [42], the large majority of the simulations performed to date have used irrotational configurations, since neutron-star viscosity is believed to be too small to tidally lock the two stars prior to merger [43,44]. At the same time, the most advanced efforts over the last couple of years have been concentrated on approaches to reduce the eccentricity of the orbits or to produce binary systems with arbitrary neutron-star spins [34,38,45–51].

In the past, the COCAL code has been used to compute quasi-equilibrium sequences for binary black holes [33,52,53], and a pointwise comparison was made with the spectral code KADATH for the gravitational fields, as well as for global quantities like the ADM mass and angular momentum, finding excellent agreement. More recently, the COCAL code has been used to compute quasiequilibrium sequences for neutron-star binaries that are irrotational or spinning, with spins aligned with the orbital angular momentum [34]; also in this case, the comparison with the LORENE code for irrotational sequences has shown excellent agreement. Overall, both sets of studies show that when considering close binaries of compact objects, be they black holes or neutron stars, the use of COCAL has led to agreement in the global quantities within less than 0.03%, while for the individual metric components the differences were less than 1%.

In this work we focus on neutron-star binaries and perform a close comparison with another spectral code, LORENE, not only for the data on the initial slice, but also for their subsequent evolution. More specifically, given irrotational binaries of neutron stars produced by either LORENE or COCAL, we consider the same physical initial data in terms of gravitational mass, rest mass, and orbital frequency, and we evolve both sets of initial data with the high-order code WHISKYTHC [54–56]. The evolutions are performed at a number of resolutions, the highest of which have spacings of  $\delta x = 0.1 M_{\odot} \simeq 150 \text{ m}$  and represent a major computational cost, which has been used in Ref. [56] only for a single binary and is referred to as "very high." Across all simulations, we have monitored in detail the violations of the constraint equations, and we have performed a gravitational-wave analysis with respect to the phase of the  $\ell = m = 2$  mode of the Weyl scalar  $\Psi_4$ .

Although *global* measurements, like mass and angular momentum, show differences that are  $\lesssim 0.02\%$ , *local* (i.e., pointwise) comparisons of initial-data quantities, such as rest-mass density, extrinsic curvature, and angular velocity,<sup>3</sup> show differences that are  $\lesssim 1\%$ . Furthermore, while the calculated waveforms have only very small differences, with convergence properties that are almost identical for the two sets of initial data, we find that the Richardson-extrapolated gravitational-wave phases differ by about 1.4 radians at the merger time, after  $\sim 3$  orbits.<sup>4</sup> Stated differently, a relative difference of  $\sim 0.02\%$  in those global initial-data quantities that are normally used as a reference in neutron-star binary simulations (i.e., the mass and angular momentum), can lead to relative phase differences of  $\sim 3.5\%$ .

Given the strict restrictions for gravitational-wave data analysis [57], these results highlight the extra care needed when computing waveforms of neutron-star binaries spanning tens of orbits. More importantly, because this is the first time that evolutions from different initial-data solvers are presented, our results issue a warning signal about the importance of using initial data that is pointwise the

same when comparative studies of neutron-star binary evolutions, such as the ones carried out in Refs. [58,59], are performed.

The plan of the paper is as follows: In Sec. II we provide a review of the quasi-equilibrium equations and present the COCAL driver to the CACTUS [60] infrastructure, while in Sec. III we describe the techniques developed to import the initial data produced by COCAL in an evolution code, performing a global and local close comparison of an irrotational binary as computed with LORENE and with COCAL. Section IV is instead dedicated to the detailed comparison of the evolution of the two sets of initial data for the various configurations considered and to the presentation of the corresponding convergence properties. Finally, our conclusions are presented in Sec. V. As complementary material, we present in the Appendix a short study for corotating initial data produced by COCAL and LORENE, again at 45 km, mostly as a benchmark of future arbitrary spinning binaries.

Hereafter, spacetime indices running from 0 to 3 will be indicated with Greek letters, while spatial indices running from 1 to 3 will be indicated with Latin letters. The metric has signature (-,+,+,+,), and we use a set of geometric units in which  $G=c=M_{\odot}=1$ , unless stated otherwise (we recall that in these units  $1M_{\odot}=4.92674~\mu s=1.477~km$ ).

# II. REVIEW OF THE QUASI-EQUILIBRIUM EQUATIONS

In this section, we only state the basic definitions and equations that are solved; we refer the reader to Ref. [34] and references within for more details. The spacetime metric in a 3 + 1 decomposition is written as

$$ds^2 = -\alpha^2 dt^2 + \gamma_{ij} (dx^i + \beta^i dt) (dx^j + \beta^j dt), \quad (1)$$

where  $\alpha$ ,  $\beta^i$ , and  $\gamma_{ij}$  are, respectively, the lapse function, the shift vector, and the three-metric on some spacelike slice  $\Sigma_t$ , which is taken to be conformally flat:

$$\gamma_{ij} = \psi^4 \delta_{ij}. \tag{2}$$

Here we use the Cartesian components of the shift. The extrinsic curvature is defined as  $K_{\alpha\beta} := -\frac{1}{2} \mathcal{L}_n \gamma_{\alpha\beta}$ , where  $\mathcal{L}_n$  is the Lie derivative along the (timelike) unit vector normal  $\mathbf{n}$  to  $\Sigma_t$ . The assumption of stationarity,  $\partial_t \gamma_{\alpha\beta} = 0$ , yields  $K_{ij} = \frac{1}{2\alpha} \mathcal{L}_{\beta} \gamma_{ij}$ , while when assuming maximal slicing, the conformally rescaled trace-free part of the extrinsic curvature becomes

$$\tilde{A}^{ij} = \frac{1}{2\alpha} \left( \partial^i \beta^j + \partial^j \beta^i - \frac{2}{3} \delta^{ij} \partial_k \beta^k \right) = \frac{1}{2\alpha} (\tilde{\mathbb{L}} \beta)^{ij}. \quad (3)$$

<sup>&</sup>lt;sup>1</sup>We note that this is also the first time that evolutions are carried out using initial data of any type produced with the COCAL code.

<sup>&</sup>lt;sup>2</sup>Higher resolutions have been used by other authors to study the merger of magnetized neutron-star binaries [31].

<sup>&</sup>lt;sup>3</sup>In contrast with what happens for black-hole binaries, where the angular velocity is a *global* quantity, since it is calculated, for example, from the equality of the ADM and Komar masses, for neutron-star binaries the angular velocity is a *local* quantity computed as an eigenvalue problem that results by considering the Euler integral at exactly three points, typically along the *x* axis of the neutron star (see Sec. III B of Ref. [34]).

<sup>&</sup>lt;sup>4</sup>If our analysis is restricted to the window in time over which the waveforms are convergent (and which ends a bit before the merger), then the phase difference is 0.5 radians, with a relative difference of roughly 1.6%.

Note that  $\tilde{A}_i^j = A_i^j$ . The last term in Eq. (3) is the longitudinal operator, and the tilde symbol denotes the fact that it is related to the conformally flat geometry.

With the help of Eq. (3), the constraint equations and the spatial trace of the time derivative of the extrinsic curvature (assuming  $\partial_t K = 0$ ) result in five elliptic equations for the conformal factor  $\psi$ , the shift  $\beta^i$ , and the lapse function  $\alpha$ :

$$\nabla^2 \psi = -\frac{\psi^5}{32\alpha^2} (\tilde{\mathbb{L}}\beta)^{ab} (\tilde{\mathbb{L}}\beta)^{ij} \delta_{ia} \delta_{jb} - 2\pi E \psi^5, \quad (4)$$

$$\nabla^{2}(\alpha\psi) = \frac{7\psi^{5}}{32\alpha} (\tilde{\mathbb{L}}\beta)^{ab} (\tilde{\mathbb{L}}\beta)^{ij} \delta_{ia} \delta_{jb} + 2\pi\alpha\psi^{5} (E + 2S), \quad (5)$$

$$\nabla^2 \beta^i = -\frac{1}{3} \partial^i \partial_j \beta^j + \partial_j \ln \left( \frac{\alpha}{\psi^6} \right) (\tilde{\mathbb{L}} \beta)^{ij} + 16\pi \alpha \psi^4 j^i, \quad (6)$$

where the matter sources are  $E \coloneqq n_{\alpha}n_{\beta}T^{\alpha\beta}$ ,  $S \coloneqq \gamma_{\alpha\beta}T^{\alpha\beta}$ , and  $j^i \coloneqq -\gamma^i{}_{\alpha}n_{\beta}T^{\alpha\beta}$ . The boundary conditions for the equations above are dictated by asymptotic flatness; i.e.,  $\lim_{r\to\infty}\psi=1$ ,  $\lim_{r\to\infty}\alpha=1$ , and  $\lim_{r\to\infty}\beta^i=0$ .

For the stress-energy tensor, we assume a perfect fluid with

$$T_{\alpha\beta} = (\epsilon + p)u_{\alpha}u_{\beta} + pg_{\alpha\beta} = \rho hu_{\alpha}u_{\beta} + pg_{\alpha\beta}, \quad (7)$$

where  $u^{\alpha}$  is the four-velocity of the fluid and  $\rho$ ,  $\epsilon$ , h, and p are, respectively, the rest-mass density, the total energy density, the specific enthalpy, and the pressure as measured in the rest frame of the fluid (see Ref. [61] for details). The specific internal energy e is related to the enthalpy through  $h \coloneqq (\epsilon + p)/\rho = 1 + e + p/\rho$ . The four-velocity is decomposed as  $u^{\alpha} = u^{t}(t^{\alpha} + v^{\alpha})$  or  $u^{\alpha} = u^{t}(k^{\alpha} + V^{\alpha})$ , which correspond to an inertial frame or the corotating frame decomposition, respectively. For the fluid variables, we assume helical symmetry,

$$\mathcal{L}_{\mathbf{k}}(hu_{\alpha}) = \mathcal{L}_{\mathbf{k}}\rho = 0, \tag{8}$$

where

$$k^{\mu} := t^{\mu} + \Omega \phi^{\mu} \tag{9}$$

is the helical Killing vector, and without loss of generality,

$$\phi^i = (-y, x, 0) \tag{10}$$

is the rotational generator. For corotating binaries,  $V^{\alpha}=0$ , and the Euler equation results in a first integral

$$\frac{h}{u^t} = C$$
, with  $u^t = \frac{1}{\sqrt{\alpha^2 - \omega_i \omega^i}}$ , (11)

where  $\omega^i := \beta^i + \Omega \phi^i$  is the corotating shift. For irrotational binaries,  $hu_\alpha = \nabla_\alpha \Phi$ , with  $\Phi$  being the fluid velocity potential, and the first integral of the Euler equation is

$$\frac{h}{u^t} + V^j D_j \Phi = C, \qquad h = \sqrt{\lambda^2 / \alpha^2 - D_i \Phi D^i \Phi}, \quad (12)$$

with  $\lambda := C + \omega^i D_i \Phi$ . The fluid potential  $\Phi$  is determined from the conservation of rest mass,  $\nabla_{\alpha}(\rho u^{\alpha}) = 0$ , which yields

$$\nabla^2 \Phi = -\frac{2}{\psi} \partial_i \psi \partial^i \Phi + \psi^4 \omega^i \partial_i (h u^i)$$
  
+  $[\psi^4 h u^i \omega^i - \partial^i \Phi] \partial_i \ln \left( \frac{\alpha \rho}{h} \right),$  (13)

with the boundary condition on the star surface

$$[(\psi^4 h u^t \omega^i - \partial^i \Phi) \partial_i \rho]_{\text{surf}} = 0. \tag{14}$$

This condition is derived either from Eq. (13), assuming that the baryon density vanishes on the stellar surface, or by demanding that the fluid velocity be tangent to the stellar surface in the corotating frame  $[V^{\mu}\nabla_{\mu}\rho]_{\rm surf}=0$ . Equations (4)–(6) will be solved together with (11) for corotating motion or with (12) and (13) for irrotational motion, and the two involving constants  $\Omega$ , C will be determined in the process. Details about the methods we use in COCAL to solve these equations are described in Ref. [34].

## III. INITIAL DATA IMPORT AND COMPARISON

COCAL uses finite differences on spherical coordinates to compute the various field variables. Importing the initial data into an evolution code involves interpolating from the COCAL grid to the one used by the evolution code, which in most cases is in Cartesian coordinates. In this section we describe the COC2CAC driver, which interpolates the COCAL grid variables to the EINSTEIN TOOLKIT [62,63]. The full description of the coordinate systems used by COCAL can be found in Ref. [52] for black-hole binaries or Ref. [34] for neutron-star binaries. Here, we review the most salient features that will be necessary for the COC2CAC driver.

### A. The COC2CAC driver

As is customary in a 3+1 decomposition, the spacetime manifold  $\mathcal{M}=\mathbb{R}\times\Sigma_t$  is foliated by a family of spacelike hypersurface  $\Sigma_t$ , parametrized by  $t\in\mathbb{R}$ . These hypersurfaces may represent data that are stationary (in equilibrium) or quasi-stationary (in quasi-equilibrium), and they are covered by overlapping multiple spherical coordinate patches. In Fig. 1, three such coordinate systems are used to cover the hypersurface. One can think of Fig. 1 as the

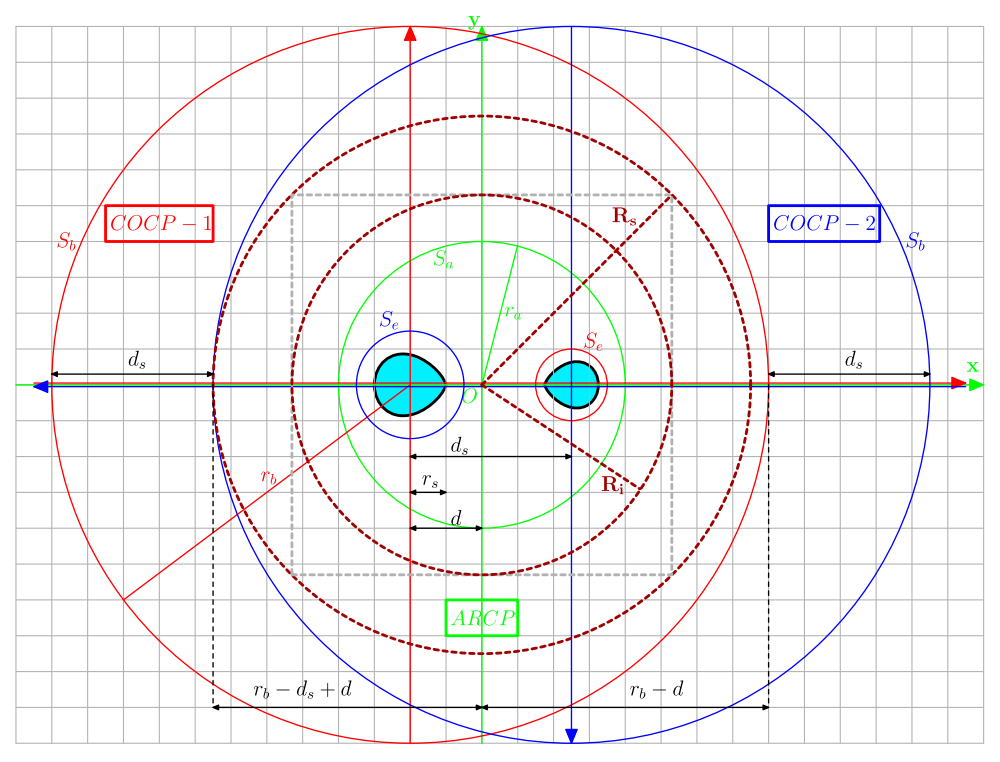


FIG. 1. Structure of a two-dimensional cross section of the COCAL grids (colored spherical coordinates) overlaid on a Cartesian coordinate system used for the evolution of the initial data. Here we assume that the z=0 plane of the evolutionary grid coincides with the corresponding COCAL plane. Evolution gridpoints  $P(x_p, y_p, z_p)$  inside the sphere of radius  $R_i$  are interpolated from the coordinate patches COCP-1 or COCP-2 depending on whether  $x_p \le 0$  or  $x_p > 0$ . Points outside that sphere are interpolated from the asymptotic region patch ARCP. Note that the figure is not to scale; in particular, the size of the sphere of radius  $R_i$  is much larger than the size of the inner boundary  $S_a$  of ARCP. The outer boundary of ARCP is not shown here and extends to very large values when compared to the compact-object sizes. Typical values are  $r_b=100$ ,  $d_s=2.5$ , d=1.25,  $R_s=98.75$ ,  $R_i=69.125$ , and  $r_a=5.0$ . The point where the neutron star's surface intersects the positive x axis of the COCP takes values  $r_s \le 1$  and is in general different for the two stars. The cusps that appear in the figure are pictorial and do not represent any model used in this work.

equatorial plane of a neutron-star binary system. Two spherical coordinate patches are used to cover the area around each neutron star. They are called COCP-1 and COCP-2 (from compact object coordinate patch) and are plotted with red and blue colors, respectively. COCP-1 (COCP-2) includes all points inside the outer red (blue) sphere  $S_b$  of radius  $r_b$ , but outside the red (blue) excised sphere  $S_e$ . Note that these two systems have opposite (x, y)coordinates, but the same z orientation. The reason for introducing the excised sphere  $S_e$  [64] is to be able to resolve the second compact object with reasonable resources. Without it, the size of the companion neutron star has to be resolved by angular grids, while by using this concept, it is enough to resolve the size of  $S_e$ , which is  $\sim d_s/2$ . This implies that the angle to be resolved is  $\sim 2 \arcsin 1/2 = \pi/3$ . As a rule of thumb, the angular resolution of a COCP is determined from the degree of accuracy to resolve the deformation of the neutron stars centered at the patch, and to resolve the size of their excised

sphere. The third patch, called the asymptotic region coordinate patch or ARCP, is denoted by green lines and includes all points outside the sphere  $S_a$  and infinity, typically a sphere  $S_b$  not shown here at a very large distance from the center of mass O.

The values of the radii  $r_a$ ,  $r_b$ , and  $r_e$  that correspond to spheres  $S_a$ ,  $S_b$ ,  $S_e$  for each of the coordinate patches used are set as follows. For the case of ARCP, the radius  $r_a$  of the inner boundary  $S_a$  is taken to be large enough to be placed outside of the excised spheres  $S_e$  for each COCP, but small compared to the radius  $r_b$  of the outer boundary  $S_b$  for each COCP. Typically, for a neutron star with a mass M,  $r_b = \mathcal{O}(100M)$  and  $r_e = \mathcal{O}(M)$  for COCP, while  $r_a = \mathcal{O}(10M)$  and  $r_b = \mathcal{O}(10^6M)$  or larger for ARCP. At present, although no compactification of the ARCP is done, no obvious problem related to our results has been detected.

Another important feature used in COCAL, which is relevant for correctly importing the initial data to an evolution code, is the normalization of all its quantities. This is discussed in detail in Sec. III B of Ref. [34], but let us mention the most important facts. In particular, we rescale the spatial coordinates  $x^i$  as

<sup>&</sup>lt;sup>5</sup>Note that the outer radii  $r_b$  of COCP-1 and COCP-2 need not be equal, but in most cases we make such a choice.

$$\hat{x}^i \coloneqq \frac{x^i}{R_0}.\tag{15}$$

We do this in order to stabilize the root-finding method for the eigenvalues C,  $\Omega$ , the constant of the Euler integral, and the angular velocity of the compact object, as well as for controlling the star surface. For single rotating neutron stars [65,66], the rescaling factor  $R_0$  is chosen so that the coordinate equatorial radius of the star is unity (stated differently, the radius of the star along the positive x axis is  $R_0$ ). For neutron-star binaries [34], the scaling factor is chosen in such a way that the coordinate equatorial radius of the star has a fixed value  $r_s \le 1$  (stated differently, the radius of the star along the positive x axis is  $r_s R_0$ ). In typical evolution codes, such as the one employed here, the units are also  $G = c = M_{\odot} = 1$ , so that for an arbitrary point  $(x, y, z)_{cac}$ , the correspondent COCAL point is

$$(x, y, z)_{\text{cac}} \rightarrow (x, y, z)_{\text{coc}} = \left(\frac{x_{\text{cac}}}{R_0}, \frac{y_{\text{cac}}}{R_0}, \frac{z_{\text{cac}}}{R_0}\right), \quad (16)$$

and similar care has to be taken when one is taking derivatives, as, for example, in the extrinsic curvature, i.e.,

$$(K_{ij})_{\text{cac}} = \frac{(K_{ij})_{\text{coc}}}{R_0}.$$
 (17)

For simplicity, hereafter we will assume that one has taken into account the normalizing factor  $R_0$  when translating points and variables from an evolution code to COCAL, and we will describe only the choice that has to be made regarding the coordinate systems.

Figure 1 shows with a light gray color the z = 0 plane of a Cartesian grid used by an evolution code, as well as the three spherical coordinate systems that are typically used by COCAL. The hypersurface  $\Sigma_t$  where a solution is provided by COCAL has the same z = 0 plane with the evolutionary Cartesian grid whose origin is also identified by the "center of mass" O of COCAL. In other words, the asymptotic patch, ARCP, of COCAL has the same origin as the evolutionary Cartesian grid, and the z = 0 plane is the same for all grids. The problem is then to interpolate for each Cartesian gridpoint,  $P(x_p, y_p, z_p)$ , from the nearby COCAL spherical points. We note that  $(x_p,y_p,z_p)$  are also the coordinates of P with respect to ARCP. To perform such an interpolation, a choice has to be made regarding the position of P relative to the COCAL coordinate systems. Since all distances are measured with respect to O, the general rule of thumb is that if the distance  $r_p =$  $\sqrt{x_p^2 + y_p^2 + z_p^2}$  is large enough, then the interpolation will be performed in the ARCP. Otherwise, for points close to O the interpolation will be done from either COCP-1 or

COCP-2. Inside the COCPs (spheres  $S_b$  in Fig. 1), points

are not uniformly distributed and, in addition, there are

"holes", i.e., regions devoid of coordinate points, which are the regions inside the spheres labeled as  $S_e$ . One simple solution is to consider the  $x_p$  coordinate of P. If  $x_p \le 0$ , then we perform a fourth-order Lagrange interpolation from nearby COCP-1 points; otherwise we perform one from COCP-2.

As a more concrete example of the procedure followed in the driver, we can adopt the same notation as in Refs. [34,52] and denote by  $d_s$  the distance between the two stars (i.e., between the geometric centers of the two stars). We also denote by d the distance from the center of mass of the system to the geometric center of the star on the negative x axis of ARCP. Without loss of generality, we then assume that the heavier star is on the negative x axis, so that  $d_s \ge 2d$ , and that the radii  $r_b$  of COCP-1 and COCP-2 are the same (we can always make such a choice). As a result, the outermost point of COCP-2 along the negative ARCP x axis is at a distance  $r_b - d_s + d$  from O, while the outermost point of COCP-1 along the positive ARCP x axis is at a distance  $r_b - d$ . Let therefore

$$R_s := \min\{r_b - d_s + d, r_b - d\} = r_b - d_s + d, \quad (18)$$

and consider the cube centered at O with each face having a length  $2R_i$ ,  $R_i \coloneqq R_s/\sqrt{2}$ . In practice we take  $R_i = 0.7R_s$ . Then, for each Cartesian point P, if  $r_p \ge R_i$ , we interpolate from ARCP; otherwise, we examine the sign of  $x_c$ . For  $x_c \le 0$  and  $r_p < R_i$ , we interpolate from COCP-1, while we interpolate from COCP-2 otherwise. Notice also that in a region with  $x_c \le 0$ , COCP-1 is denser than COCP-2, so the interpolations will be more accurate. The con+trary is true for  $x_p > 0$ . Typical values for the relevant quantities are  $r_b = 100$ ,  $d_s = 2.5 = 2d$ , which means that  $R_s = 98.75$ , while  $R_i = 69.125$ . As a concluding remark, we note that Fig. 1 is not to scale. For example, the inner boundary of ARCP (green sphere  $S_a$ ) has radius  $r_a = 5.0$ , so in reality, there is quite a large space between that and the sphere of radius  $R_i$ , while in the figure they appear quite close.

# B. Local and global comparison of initial data from LORENE and COCAL

In this section, we carefully compare the initial data produced by two different codes, namely COCAL and LORENE, which use completely different numerical methods for the solution of the constraint equations. In particular, COCAL is a finite-difference code, while LORENE employs pseudospectral methods. For this comparison, we compute the solutions for the physically same irrotational binary having the same gravitational (rest) mass, and where the two stars are at a distance of approximately 44.7 km. The reason we use the adverb "approximately" is because the two codes obtain the final solutions in rather different ways. On the one hand, LORENE allows one to set up explicitly the masses of the binary and the distance

TABLE I. Summary of the grid parameters used for the binary systems computed here.

$r_a$ :	Radial coordinate where the radial grids start. For the COCP patch, it is $r_a = 0$ .
$r_b$ :	Radial coordinate where the radial grids end.
$r_c$ :	Center-of-mass point. Excised sphere is located at $2r_c$ in the COCP patch.
$r_e$ :	Radius of the excised sphere. Only in the COCP patch.
$r_s$ :	Radius of the sphere bounding the star's surface. It is $r_s \le 1$ . Only in COCP.
$N_r$ :	Number of intervals $\Delta r_i$ in $r \in [r_a, r_b]$ .
$N_r^1$ :	Number of intervals $\Delta r_i$ in $r \in [0, 1]$ . Only in the COCP patch.
$N_r^{\mathrm{f}}$ :	Number of intervals $\Delta r_i$ in $r \in [0, r_s]$ in the COCP patch or $r \in [r_a, r_a + 1]$ in the ARCP patch.
$N_r^{\mathrm{m}}$ :	Number of intervals $\Delta r_i$ in $r \in [r_a, r_c]$ .
$N_{\theta}$ :	Number of intervals $\Delta \theta_i$ in $\theta \in [0, \pi]$ .
$N_{\phi}$ :	Number of intervals $\Delta \phi_k$ in $\phi \in [0, 2\pi]$ .
d:	Coordinate distance between the center of $S_a$ $(r=0)$ and the center of mass.
$d_s$ :	Coordinate distance between the center of $S_a$ $(r=0)$ and the center of $S_e$ .
L:	Order of included multipoles.

between the two stars, and an iteration is then carried out until a circular solution is obtained at the desired accuracy. In COCAL, on the other hand, distances are expressed in terms of the normalizing factor  $R_0$ , which is only found at the end of the computation. The same is true for any other quantity, such as angular velocity, mass, etc. [34].

Details of the logical flow followed by COCAL can be found in Sec. III B of Ref. [34], with the relevant radii summarized in Table I. Note that  $r_s$  is the radius that corresponds to the inner point of the neutron star's surface closer to the center of mass, and  $d_s$  is the coordinate distance between the two stars. The physical lengths, though, are  $r_sR_0$  and  $d_sR_0$ , so that as one sets the coordinate distance  $d_s$  and the star radius  $r_s$ , COCAL computes binaries whose separation is expressed in terms of the star's radius. When a converged solution is obtained, the code finds the value of  $R_0$  (as well as of  $\Omega$  and the constant of the Euler integral C) and can then compute the physical separation in km of the binary. As the resolution

changes,  $R_0$  also changes slightly, with the consequence that the distance  $d_s$  between the two stars changes too. Of course, this change is very small, and we can safely assume that the binary systems are at the same separation. In the future, we plan to address this issue by changing  $r_s$  and employing a root-finding method to arrive exactly at the requested distance between the two stars.

At present, however, we compute the initial data for an irrotational binary at separation of  $\approx$ 44.7 km by fixing  $r_s = 0.7597667$  and  $d_s = 2r_c = 2.5$ , and report in Table II the four different resolutions used by COCAL to obtain the solutions presented here. Each symbol is explained in Table I and in more detail in Ref. [34]. For simplicity, and because we are not interested in microphysical effects here, the equation of state is set to be a simple polytrope with polytropic index  $\Gamma = 2$  and polytropic constant K = 123.6.

The initial data computed by LORENE employs six different domains to cover the computational region around

TABLE II. Four different grid structure parameters used for the circular binary computation in COCAL. All variables are explained in Table I, and the distances are in normalized quantities. The COC2CAC driver interpolates from COCP-1 and COCP-2 when the normalized distance of the point under consideration from the center of mass is less than  $R_i = 69.125$ , while it interpolates from ARCP for larger values.

Type	Patch	$r_a$	$r_s$	$r_b$	$r_c$	$r_e$	$N_r^{ m f}$	$N_r^1$	$N_r^{\rm m}$	$N_r$	$N_{\theta}$	$N_{\phi}$	L
Hs2.0d	COCP-1	0.0	0.759 766 7	10 <sup>2</sup>	1.25	1.125	50	64	80	192	48	48	12
	COCP-2	0.0	0.759 766 7	$10^{2}$	1.25	1.125	50	64	80	192	48	48	12
	ARCP	5.0		$10^{6}$	6.25		16		20	192	48	48	12
Hs2.5d	COCP-1	0.0	0.759 766 7	$10^{2}$	1.25	1.125	76	96	120	288	72	72	12
	COCP-2	0.0	0.759 7667	$10^{2}$	1.25	1.125	76	96	120	288	72	72	12
	ARCP	5.0		$10^{6}$	6.25		24		30	192	72	72	12
Hs3.0d	COCP-1	0.0	0.759 766 7	$10^{2}$	1.25	1.125	100	128	160	384	96	96	12
	COCP-2	0.0	0.759 766 7	$10^{2}$	1.25	1.125	100	128	160	384	96	96	12
	ARCP	5.0		$10^{6}$	6.25		32		40	384	96	96	12
Hs3.5d	COCP-1	0.0	0.759 766 7	$10^{2}$	1.25	1.125	150	192	240	576	144	144	12
	COCP-2	0.0	0.759 766 7	$10^{2}$	1.25	1.125	150	192	240	576	144	144	12
	ARCP	5.0		$10^{6}$	6.25		48		60	384	144	144	12

TABLE III. Physical parameters of the irrotational binaries at the various resolutions of Table I. The columns denote the rest mass of each star, the ADM mass of the binary, the Komar mass, the central rest-mass density, and the ADM angular momentum in units of  $G = c = M_{\odot} = 1$ , while the angular velocity, the separation, and the equatorial radius are in physical units. The separation changes slightly with resolution as a result of the iteration procedure followed by COCAL. Similar quantities are reported for the solution computed by LORENE. The ADM mass of a spherical solution that corresponds to a rest mass  $M_0 = 1.62505$  is  $M_{\rm ADM} = 1.51481$ , and the compactness is C := M/R = 0.1401.

Code	$M_0$	$M_{ m ADM}$	$M_{ m K}$	$\rho_c \times 10^{-4}$	$J_{ m ADM}$	$\Omega[\mathrm{rad/sec}]$	$d_s[km]$	$R_{\rm eq}[{ m km}]$
COCAL Hs2.0d	1.625 04	2.997 37	2.997 16	9.563 899	8.795 53	1856.75	44.735	13.595
COCAL Hs2.5d	1.625 05	2.997 33	2.997 18	9.577 718	8.810 18	1857.29	44.722	13.591
COCAL Hs3.0d	1.625 05	2.998 17	2.998 04	9.582 239	8.820 99	1857.42	44.718	13.590
COCAL Hs3.5d	1.625 05	2.998 22	2.998 11	9.585 707	8.825 49	1857.48	44.715	13.589
LORENE	1.625 04	2.998 34		9.569 626	8.818 79	1867.49	44.707	13.605

each star, with a number of collocation points for the spectral expansion given by  $N_r \times N_\theta \times N_\phi = 33 \times 25 \times 24$ , where  $N_r$ ,  $N_\theta$ , and  $N_\phi$  denote the number of points for the radial, polar, and azimuthal directions, respectively. In our model, the ratio between the star radius and the separation is roughly 3, so that, according to Ref. [67], the resolution that we employ is sufficient to achieve a fractional error of  $10^{-5}$  in the ADM mass comparable to the one obtained by COCAL.

The physical parameters of the binary are presented in Table III. Each star of the binary is constructed to correspond to a spherical solution of rest mass  $M_0 = 1.62505$  or  $M_{\rm ADM} = 1.51481$ , with a relative accuracy of  $\mathcal{O}(10^{-6})$  in the rest mass, which is computed as

$$M_0 = \int_{\Sigma_t} \rho u^{\alpha} dS_{\alpha}, \tag{19}$$

while the ADM and Komar masses are computed as

$$M_{\rm ADM} = -\frac{1}{2\pi} \int_{S_{-}} \partial^{i} \psi dS_{i}, \qquad (20)$$

$$M_{\rm K} = \frac{1}{4\pi} \int_{S_{\infty}} \partial^i \alpha dS_i. \tag{21}$$

The surface integrals are calculated at a certain finite radius, typically around  $r \sim 10^4 M$ , and the relative differences found between the Komar and ADM masses is of the order of  $10^{-5}$  even for the COCAL initial data with the coarsest resolution Hs2.0d, thus providing a simple measure of the overall error of the code. The ADM angular momentum is instead computed as

$$J = \frac{1}{8\pi} \int_{S_{\infty}} K^a{}_b \phi^b dS_a. \tag{22}$$

In Fig. 2, we report various quantities of the irrotational solution along the positive x axis of the Cartesian grid, so that x = 0 is the center of mass of the binary. The star of

radius  $R_{\rm eq} \approx 9~M_{\odot}$  is positioned approximately at  $x \approx 15~M_{\odot}$ . In both figures, on the left column we plot the quantity as computed with COCAL (red lines) and LORENE (blue lines), relative to the Hs3.0d resolution, while on the right column we plot the relative difference

$$\Delta f := \left| 1 - \frac{f_{\text{COCAL}}}{f_{\text{LORENE}}} \right|. \tag{23}$$

Going from top to bottom in Fig. 2, the quantities plotted are the metric  $g_{xx} = \psi^4$  (note that  $g_{ij} = \psi^4 \delta_{ij}$ ), the lapse function  $\alpha$ , the y component of the shift, the xy component of the extrinsic curvature, and the rest-mass density, while Fig. 3 plots the y component of the fluid velocity with respect to the Eulerian observer and the corresponding Lorentz factor.

The four-velocity can also be written as  $u^{\mu} = \alpha u^{t}(n^{\mu} + U^{\mu})$ , with  $n^{\mu}$  the unit normal to the hypersurface (Eulerian four-velocity) and

$$U^{y} = \frac{1}{\alpha} \left( \frac{u^{y}}{u^{t}} + \beta^{y} \right) = \frac{\gamma_{\mu}^{y} u^{\mu}}{\alpha u^{t}} = \alpha \frac{\psi^{-4} \partial^{y} \Phi}{\lambda}, \quad (24)$$

where we recall that  $\lambda := C + \omega^i D_i \Phi$ . As can be seen in Fig. 3, the difference in the computed variables between the two codes is of the order of 1% or less, except for points at or near zero crossings, where the relative error, Eq. (23), produces large values.

Comparing the right column of Fig. 2 with that of Fig. 6 of Ref. [33], where a similar comparison was made between COCAL and KADATH for black-hole binary initial data, we note that the difference between the two codes is approximately 1 order of magnitude larger than in Ref. [33]. There are two main reasons behind this.

First, in Ref. [33], the comparison was direct in the sense that the KADATH code evaluates the solution at exactly the same gridpoints used by COCAL, so that no interpolation needs to be done; here, on the other hand, the comparison is done after the solutions of both LORENE and COCAL are interpolated on the Cartesian grids. Second, and more importantly, the black-hole binary problem is scale free,

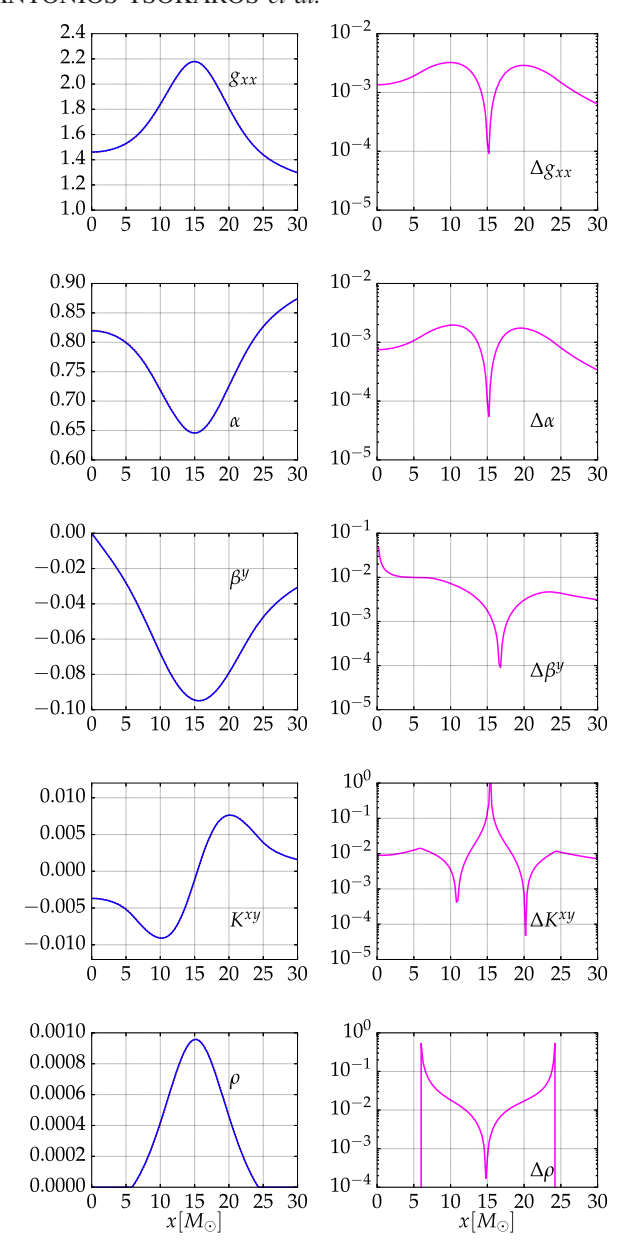


FIG. 2. Left column: From top to bottom, initial data quantities relative to the metric function  $g_{xx} = \psi^4$ , the lapse function  $\alpha$ , the y component of the shift, the xy component of the extrinsic curvature, and the rest-mass density  $\rho$ , as computed by COCAL (red lines) and LORENE (blue lines). The x axis is the positive x axis of the Cartesian grid, with x = 0 corresponding to the center of mass of the binary. Right column: Relative difference between COCAL and LORENE as computed from Eq. (23).

thus allowing Ref. [33] to compare *exactly* the same physical system. This is no longer true for the neutron-star binaries that we explore here, since the two binaries have slightly different central rest-mass densities and also different separations, radii, etc. (see Table III). This is also manifested by the fact that Figs. 2 and 3 do not change considerably if we increase or decrease the COCAL resolution, implying that the observed differences in the metric

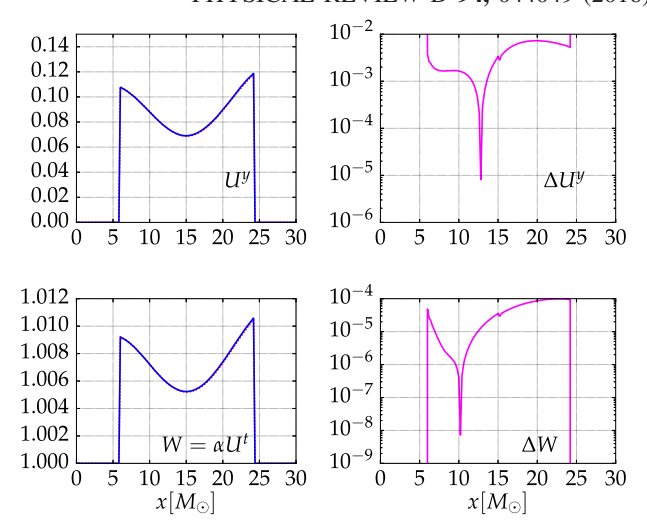


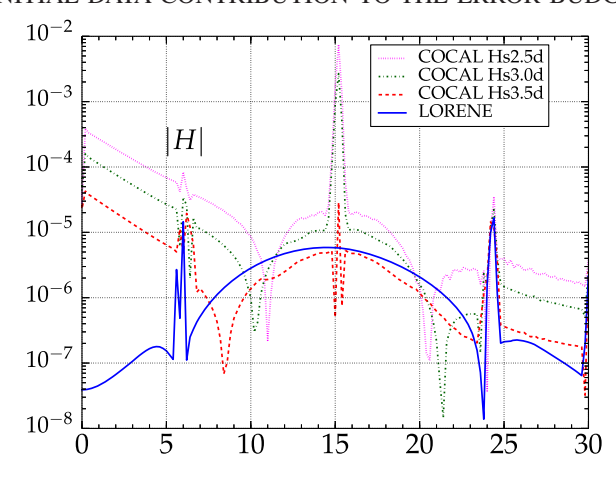
FIG. 3. The same as Fig. 2 for the *y* component of the three-velocity relative to the Eulerian observers and the corresponding Lorentz factor.

functions are already dominated by the intrinsic differences in the physical models considered.

Having examined some of the representative variables of the initial-data set, we next move into an analysis of the constraint equations on the initial spacelike hypersurface. In Fig. 4, we show the residuals for both the Hamiltonian constraint equation and the y component of the momentum-constraint equation along the x axis. Here too, x=0 corresponds to the center of mass of the binary, with the star surface located at  $x\approx 6~M_{\odot}$  and at  $x\approx 24~M_{\odot}$ . For the initial data computed with COCAL, we show the three highest resolutions Hs2.5d, Hs3.0d, Hs3.5d of Table I and note that since the star radius is 13.59 km and the number of points across the star are  $N_r^f=76$ , 100, and 150 at these three resolutions, the spatial resolution along the x axis is 179, 136, and 91 m, respectively.

A first reading of these plots reveals that inside the star, both codes produce errors of approximately the same magnitude. For COCAL, however, the Hamiltonian violations have a spike at the center of the star, i.e., at  $x \approx 15~M_{\odot}$ , which converges away with increasing resolution (cf. initial-data set Hs3.5d). This spike, which involves ~4–5 points around the center, is not a reason of major concern for two distinct reasons. First, the localized violation is rapidly removed when the initial data are actually evolved, leaving no apparent influence on the evolution (see also the discussion in Sec. IV).

Second, as we can see from Fig. 2, the conformal factor  $\psi$  is computed very accurately in the region around the stellar center; indeed, a closer inspection of the terms that produce this violation reveals that it is the result of the location of the origin of the spherical COCP, which induces local inaccuracies in the second spatial derivatives of the conformal factor,  $\partial_i^2 \psi$ , near the stellar center.



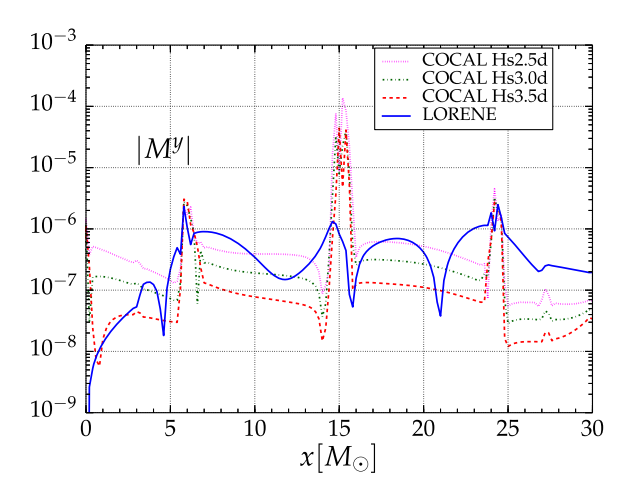


FIG. 4. Hamiltonian (top) and momentum-constraint violations (bottom) for the y component of the shift ( $\beta^y$ ) along the x axis for the irrotational binary system at the initial time. The origin x=0 corresponds to the center of mass of the binary, with the surface of the star to be located at  $x \approx 6 \ M_{\odot}$  and at  $x \approx 24 \ M_{\odot}$ .

Similarly, the violations of the momentum constraint inside the star are of the same order as (or even smaller than) those produced by LORENE. Around the stellar surface, both codes exhibit a jump in the violations due to the existing discontinuity in the first derivatives of the matter fields. Outside the star and towards the center of mass, the COCAL code produces violations that are 3 orders of magnitude larger than those produced by LORENE in the Hamiltonian constraint, but of the same order for the momentum constraint. The reason for this behavior is probably to be found in the resolution of the radial grid, since in that region we have an increasing step of  $\delta x$ . We plan to study the source of this error in the future by modifying the grid structure there. From the opposite side of the star and moving towards spatial infinity, again we have a reasonable agreement between the three sets of initial data. It is also important to notice that the COCAL violations converge away with the expected second-order accuracy of the finite-difference scheme.

# IV. IMPACT ON THE EVOLUTIONS OF DIFFERENT INITIAL-DATA SOLVERS

In order to evolve the initial-data sets introduced in the previous section, we have used the high-order evolution code WHISKYTHC [54–56], which solves the equations of generalrelativistic hydrodynamics in the *Valencia formulation* [68] using a finite-difference scheme that reconstructs the fluxes in local-characteristic variables using a high-order reconstruction scheme (MP5 [69]). In these simulations, we also employed a positivity-preserving limiter, which is crucial to treat properly the low-density regions of the flow [54]. The evolution of the spacetime is provided by the MCLACHLAN code [70], which solves a conformal-traceless "3 + 1" formulation of the Einstein equations either in the BSSNOK [71–73] or in the CCZ4 form [74]; we have here employed the BSSNOK formulation, leaving to future work the investigation with the CCZ4 formulation. The MCLACHLAN code is part of the open-source software framework EINSTEIN TOOLKIT [62,63], which is based on the CACTUS [60] computational toolkit. We use a fourth-order finite differencing and the very robust Gamma-driver shift condition together with the " $1 + \log$ " slicing, which have been shown to be numerically well behaved for spacetimes describing both isolated and neutron-star binaries [23,75,76].

In particular, we use for these simulations a computational domain in which  $0 < x, z \le 1024~M_{\odot}$  and  $-1024~M_{\odot} \le y \le 1024~M_{\odot}$ ; i.e., we assume  $\pi$  symmetry along the (x,z) plane and reflection symmetry on the (x,y) plane. It is important to remark that placing the outer boundary at a sufficiently large radius is crucial to avoid the possibility of spurious and constraint-violating reflections from the outer boundaries spoiling the convergence order. For example, we have experienced that having a computational domain with the outer boundary at 512  $M_{\odot} \simeq 755~{\rm km}$ , which is quite common for neutron-star binary simulations [77], would not yield convergence waveforms.

An adaptive mesh-refinement grid (AMR) hierarchy is provided by the CARPET driver [78,79], and we use six levels of refinement, the finest of which has three different resolutions: low (L), medium (M), and high (H). These three resolutions correspond, respectively, to spatial mesh spacings of  $h=0.2,0.133,0.1~M_{\odot}\simeq 295,197,148$  m, or, equivalently, to 80, 120, and 160 cells along the x axis for the coarsest grid. See Table IV for more details on this grid hierarchy.

The initial data, computed with either LORENE or COCAL (for the latter, we use the Hs3.5d data set), are then evolved with a Courant factor set to 0.3. We note that we reset the shift vector to zero at the start of each evolution; i.e., we do not use the shift as provided by the initial-data codes. The two stars inspiral for about three orbits (i.e., approximately seven gravitational-wave cycles) and then merge. Because the initial masses have been chosen to be sufficiently large, the merger leads to a prompt collapse to a black hole surrounded by an accretion torus [23].

TABLE IV. AMR grid hierarchy: Reported are the boxes' extents along the x, y, and z directions, which reflect the symmetry conditions imposed on them, i.e.,  $\pi$  symmetry along the x coordinate at x=0 on the (y,z) plane; reflection symmetry along the z coordinate at z=0, i.e., on the (x,y) equatorial plane. The grid hierarchy was kept fixed throughout the simulation for each one of the different simulations. The mesh spacings listed in the last column are the ones used for the highest-resolution simulation.

			Mesh spacing	
Level	x	У	z	h
0	[0, 1024]	[-1024, 1024]	[0, 1024]	3.2
1	[0, 240]	[-240, 240]	[0, 240]	1.6
2	[0, 120]	[-120, 120]	[0, 120]	0.8
3	[0, 64]	[-64, 64]	[0, 48]	0.4
4	[0, 40]	[-40, 40]	[0, 22]	0.2
5	[0, 30]	[-30, 30]	[0, 11]	0.1

A more complete picture of the constraint violations as a function of time is shown in Fig. 5, where each panel shows the constraint violations in the equatorial plane, or (x, y)plane, of the binary, focusing on the region from the center of mass (middle of the left side on each panel) to approximately six neutron-star radii. From top to bottom, the first row represents COCAL Hs3.0d initial data, while the second row shows the LORENE Hamiltonian violations at three different times: at t = 0, which corresponds to the initial data, just after the simulation is launched, at  $t = 30.72 M_{\odot}$ , and after one orbit, at  $t = 660.48 M_{\odot}$ . When considering the properties of the initial data, it is possible to note the characteristic spherical-coordinate pattern of COCAL, while in the case of LORENE data, one has a wavy kind of structure which reflects the spectral methods used. The surface of the neutron star is easily noticeable, as violations of the constraints tend to create a discontinuity there. Also visible is the increase of COCAL's violations towards the center of mass as was seen in Fig. 4. Apparently these violations exist in the region around the (y,z) plane close to the center of mass. The small spike of violations at the center of the neutron star is also visible.

Soon after the beginning of the evolution, at  $t=30.72~M_{\odot}$  (middle column), the stars have rotated about 10 degrees, and the violations of both codes become very similar both inside the star as well as near the center of mass. This tendency continues one orbit afterwards (third column) at  $t=660.48~M_{\odot}$  up until the merger. In the third and fourth rows, we show the momentum violations for COCAL and LORENE, respectively. Again the characteristic patterns of both codes are visible in the initial data of the first column, with COCAL having fewer violations inside and around the star. As the binary evolves, differences are washed out, and both codes produce similar behaviors.

Up until now all convergence analysis has been done with respect to the resolution of the initial data. In what follows,

we fix the initial data (Hs3.5d for COCAL) and perform a convergence analysis with respect to the resolution of the evolution code. In Fig. 6, we monitor the  $L_2$  norm indicator for the Hamiltonian (first row) and the y component of the momentum constraint (second row). It is defined as

$$|f|_2 := \sqrt{\frac{1}{N} \sum_{i=1}^{N} |f_i|^2},$$
 (25)

where  $N=N_r\times N_\theta\times N_\phi$  is the total number of points. Merger happens at approximately 1600  $M_\odot$  or 8 ms.

Every plot has three solid lines that correspond to the three different evolution resolutions: red is for low, green is for medium, and blue is for high, with outer boundaries at  $1024~M_{\odot}$  as stated earlier. Among the first features to be noticed in these plots are the presence of a local maximum around  $180~M_{\odot}$  and the behavior of the violations until that time. It is possible to see in Fig. 6 that this maximum is reduced as the resolution of the evolution increases, and that its position in time changes as the position of the second AMR refinement boundary is varied. Together, these considerations clearly indicate that the first local maximum in the constraint violations is simply due to the position of the second AMR box and, albeit annoying, it has a clear origin and is not particularly harmful for the subsequent evolution.

Another feature to notice when considering the constraint violations in the time interval  $0 < t < 180 M_{\odot}$  is that although the ones coming from the Hamiltonian equation scale according to the resolution (except for an initial interval  $0 < t < 50 M_{\odot}$ ), this is not happening for the momentum-constraint equation. There, the violations monotonically decrease until the starting of a "bump" at  $t = 180 M_{\odot}$ , and increasing the resolution does not affect them. At the moment we do not have a clear understanding of this behavior, which cannot be attributed to either of the numerical schemes employed (finite difference or pseudospectral), since it is present both in the COCAL and LORENE data sets. However, we do conjecture it is related to the "mismatch" between the set of equations solved for the initial data and those employed to evolve the system; inevitably, this mismatch manifests itself in the early evolution of the system. In particular, we speculate that the initial-value problem solved here relies on assumptions, such as those of a conformally flat geometry or a maximum slicing K = 0, that are no longer satisfied from the full solution of the constraint equations as monitored by our evolution code (cf. Fig. 6). These violations do not really

<sup>&</sup>lt;sup>6</sup>For example, one of the equations in the BSSN formulation involves the evolution of the trace of the extrinsic curvature K. When solved, this equation leads to a variation of K and therefore introduces terms in the constraint equations that are not present in the elliptic solvers of COCAL or LORENE.

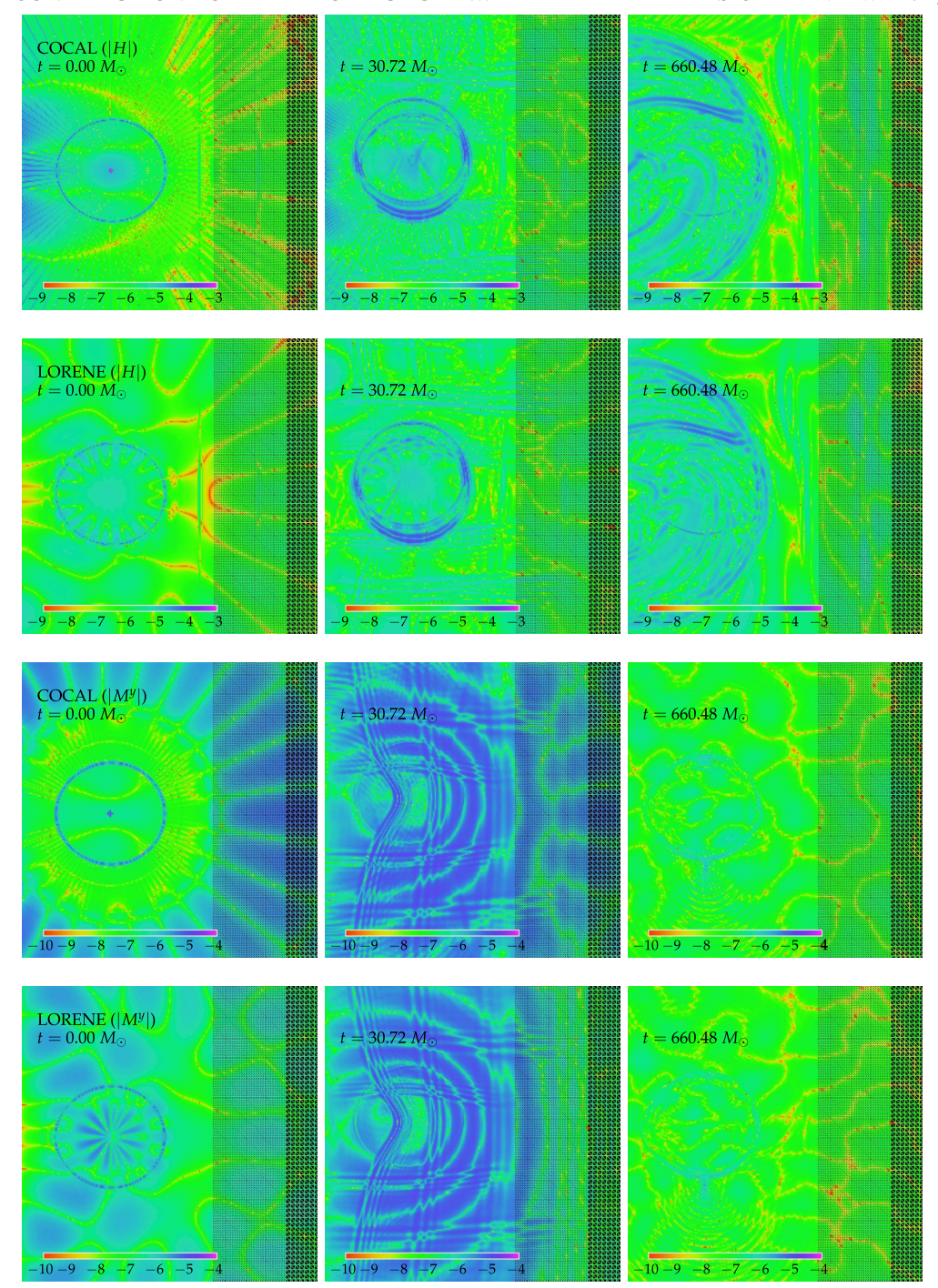


FIG. 5. Logarithmic violations of the constraint equations shown at three different times in the different columns: initial time (t=0), just after the beginning of the evolution  $(t=30.72~M_\odot)$ , and one orbit later  $(t=660.48~M_\odot)$ . From top to bottom, the first row shows the violations of the Hamiltonian constraint on the (x,y) plane from COCAL, while the second row shows the corresponding violations from LORENE. The third and fourth rows show the violations of the y component of the momentum constraint from COCAL and LORENE, respectively. Note that all panels show data on the three finest levels of refinement, with two borders clearly visible. The bounding box in the (x,y) plane encompassing each of the panels spans roughly the range  $[0,50]\times[-25,25]M_\odot$ . The oval shape indicates the neutron-star surface at every moment.

depend on the resolution of the evolution code (all lines essentially overlap in the early stages of the evolution) and are more severe for those constraint equations involving the bulk motion of the stars—namely, the momentum

constraints. Support for this conjecture comes from the fact that as the binaries are evolved in time and the fluid configurations reach a self-consistent equilibrium, the loss of convergence disappears, and the evolutions for both the

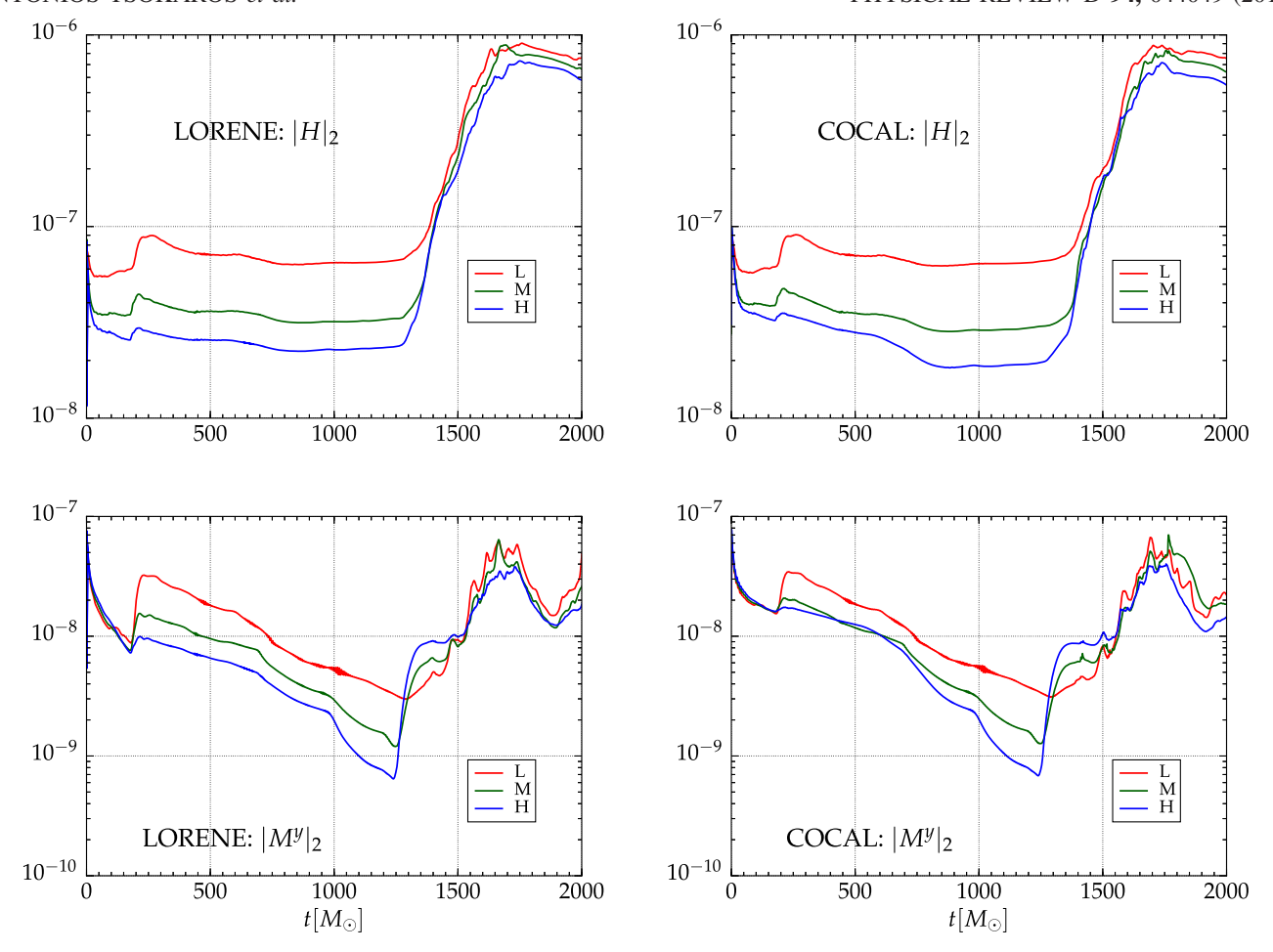


FIG. 6. Constraint violation  $L_2$  norms for COCAL and LORENE as a function of time. The first row shows the Hamiltonian constraint, while the second row represents the y component of the momentum constraint. Each color refers to a given resolution for the evolution grid: low (red), medium (green), and high (blue).

COCAL and LORENE data sets show the expected convergence rate. Proving this conjecture is not trivial and is left for future investigations.

After a certain time (180  $M_{\odot}$  for LORENE, and 800  $M_{\odot}$  for COCAL), this violation degeneracy is broken as the truncation errors from coarser grids start to dominate the error budget in the  $L_2$  norm computation, and then evolution errors start to scale with resolution as expected from the discretization scheme.

In addition to the  $L_2$  norm shown here, we have also computed and studied the behavior of the  $L_1$  norm (i.e.,  $|f|_1 \coloneqq \sum_{i=1}^N |f_i|/N$ ) and that of the  $L_\infty$  norm (i.e.,  $|f|_\infty \coloneqq \max_i \{|f_i|\}$ ). More specifically, the  $L_1$  norm is of the order of  $\lesssim 10^{-8}$  for all the resolutions considered, both for the COCAL and for the LORENE initial data, while the  $L_\infty$  norm is the largest of all, with values of the order of  $\lesssim 10^{-6}$ . This quantity, however, also shows a clear convergence scaling in the Hamiltonian violations. Overall, it is evident that the behavior of the evolution of the constraint violations is extremely similar for both COCAL and LORENE initial data.

One of the main goals in this work is to estimate the impact that slightly different initial data coming from different codes can have on the observed gravitational-wave signal. It is well known that the Einstein equations are highly nonlinear, and it is therefore possible that even minute differences in the initial data can result in large and, indeed, measurable differences in the radiated quantities. The ability to measure the size of this impact is, of course, essential in order to weigh it in with the overall budget of numerical-relativity calculations, and hence to measure how the extraction of physical parameters of the sources can be affected. Hence, we next concentrate here on the gravitational-wave emission on the  $\ell=m=2$  mode of the Weyl scalar  $\Psi_4$ , which we extract at  $\bar{r}=450~M_{\odot}$ :

$$(\Psi_4)_{22} = A(t)e^{i\phi(t)}. (26)$$

The real part of  $(\Psi_4)_{22}$  with respect to the retarded time  $t - r_{\star}$  is plotted in the top row of Fig. 7, where

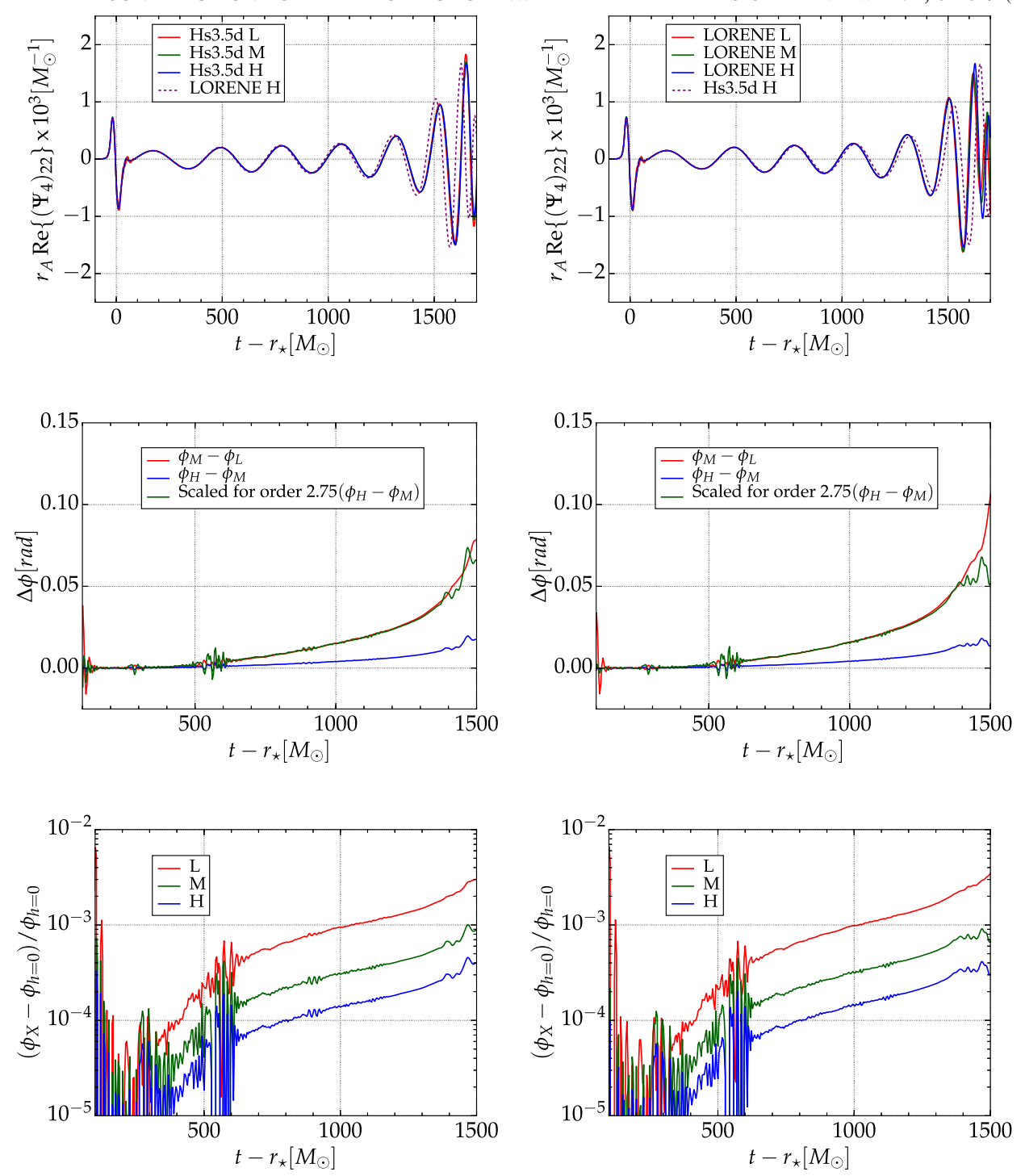


FIG. 7. First row: Real part of  $(\Psi_4)_{22}$  extracted at  $\bar{r}=450~M_\odot$  as a function of the retarded time for both COCAL Hs3.5d (left panel) and LORENE (right panel) initial data and for the three evolution resolutions (L, M, H). On each plot, the dashed line denotes the evolution with the highest resolution of the other code initial-data set so that the dephasing between the two data sets becomes apparent. Second row: Dephasing between different resolutions and the rescaled dephasing between the high and medium resolutions, assuming a convergence order p=2.75. The left panel is for COCAL, while the right one is for LORENE. Third row: Relative phase difference for the  $\ell=m=2$  mode of  $\Psi_4$  with respect to the Richardson-extrapolated value (computed assuming a convergence order of p=2.75).

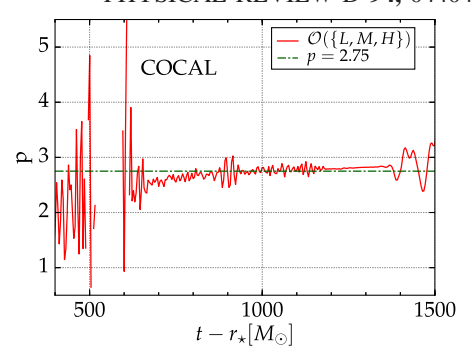
$$r_{\star} := r_A + 2M_{\text{ADM}} \ln (r_A / 2M_{\text{ADM}} - 1) \approx 478.8 \ M_{\odot}$$
 (27)

is the tortoise radius and  $r_A := \bar{r}(1 + M_{\rm ADM}/2\bar{r})^2$  is the approximated areal radius.

The left panel in the top row of Fig. 7 refers to the COCAL Hs3.5d initial data, and we report the waveforms as computed at the three different resolutions L (red line), M (green line), and H (blue line), which, we recall, are relative to spatial mesh spacings of 0.2, 0.1333, and 0.1  $M_{\odot}$  on the finest grid. Note that at these resolutions the differences among the various waveforms are extremely small, both in phase and in amplitude, and one needs to zoom in on the figure to appreciate them. Similar waveforms are shown in the right panel in the top row of Fig. 7, which instead refers to the LORENE initial data. On each of these plots we also include a dashed magenta line with the highest-resolution run of the other initial-data set in order to emphasize the dephasing that is instead observed when comparing the two initial-data sets.

This dephasing observed in the top row of Fig. 7 is reminiscent of the behavior observed in Ref. [55], where a comparison between two evolution codes of different convergence order, WHISKY [23,76] and WHISKYTHC, has been made. In that work, it was shown that given the exactly same initial data, a second-order evolution code (WHISKY) produces a significant phase difference for the gravitational wave at different resolutions. This phase difference was as large as ~2 radians between a low- and a high-resolution simulation. When the same experiment was repeated using the higher-order WHISKYTHC code, the dephasing between different resolutions became as small as ~0.6 radians. Here, the evolution runs have been done with WHISKYTHC only, and the small differences in phase are due uniquely to small differences in the initialdata sets. In other words, the evolution of the two slightly different initial-data sets resembles the dephasing measured when using evolution codes with different orders of accuracy.

To gain a better understanding of the dephasing and to compare the convergence properties for both sets of initial data, we report the change  $\Delta\phi$  between medium and low, as well as that between the high and medium resolutions, in the middle row of Fig. 7. The left plot refers to the COCAL initial data, while the right plot refers to the LORENE initial data. Also plotted is the rescaled  $\Delta\phi$  for the high-minus-medium resolution, after employing a convergence order of p=2.75 (see Fig. 8 and the discussion below). This exponent p is a



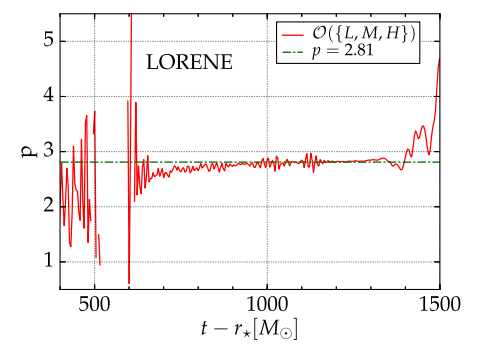


FIG. 8. Convergence order p as a function of time as computed by Eq. (28) for COCAL (top panel) and LORENE (bottom panel) initial data. The average values for COCAL (LORENE), i.e.,  $p=2.75\pm0.16$  (2.81  $\pm$  0.18), are computed as arithmetic averages over the time interval  $[650,1500]M_{\odot}$ , where outlier data points p<1 and p>4 are excluded from the average and represent the uncertainty range.

genuine measure of the convergence order of our code, and we believe similar measurements should accompany any work reporting high-quality gravitational waveforms. Here, p has been computed by solving the equation [54,61]

$$\frac{\phi_{h_1} - \phi_{h_2}}{\phi_{h_2} - \phi_{h_3}} = \frac{h_1^p - h_2^p}{h_2^p - h_3^p},\tag{28}$$

where  $(h_1, h_2, h_3) = (0.2, 0.1333, 0.1)$  are the intervals of the three resolutions L, M, and H employed. Note that because p is a function of time (see Fig. 8), the value reported refers to the average over time of all convergence orders, after discarding an initial noisy time interval, and the evolution around the merger, when the convergence is lost (see discussion in Ref. [19]). In this way, we obtain  $p = 2.75 \pm 0.16$ for the COCAL initial data and essentially the same value,  $p = 2.81 \pm 0.18$ , for the LORENE initial data. A convergence order of this magnitude is consistent with previous studies [55] of binaries at close separations. In the last row of Fig. 7 (again, the left plot refers to COCAL, while the right plot refers to LORENE initial data), we calculate the relative difference between the Richardson-extrapolated phases for the three resolutions

<sup>&</sup>lt;sup>7</sup>We have compared this approximation against a numerical computation of the areal radius based on the proper area computation of the extraction surfaces. For a surface at  $\bar{r} = 450~M_{\odot}$ , the relative differences between the approximation and the numerically computed radius was ~2 × 10<sup>-6</sup> during the inspiral and around ~4 × 10<sup>-5</sup> as it peaks during the merger.

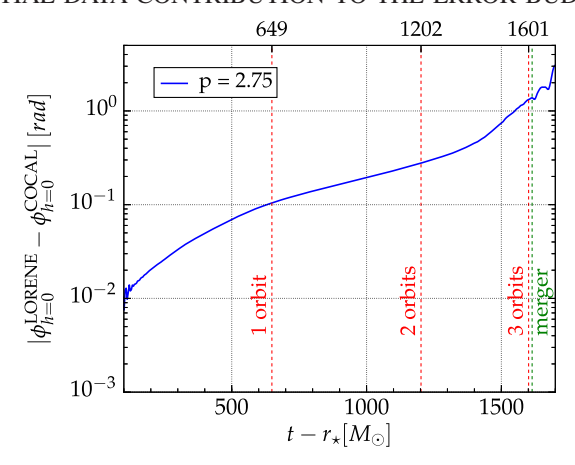


FIG. 9. Difference between the Richardson-extrapolated phases for COCAL and LORENE initial data using the three resolutions L, M, and H. Shown with dashed vertical lines are the times relative to one, two, and three orbital periods, while the green vertical line at  $t-r_{\star}=1614~M_{\odot}$  marks the merger—i.e., the time when  $|\Psi_4|$  reaches its first maximum.

used. The value at infinite resolution (h = 0) is calculated from Eq. (28) by setting, for example  $h_1 = 0$ , and solving for  $\phi_{h_1}$ . Using the previously calculated convergence order p = 2.75, this is computed as

$$\phi_{h=0} = \phi_{h_2} + \frac{\phi_{h_2} - \phi_{h_3}}{(h_3/h_2)^p - 1}.$$
 (29)

In Fig. 9, we plot the difference between the Richardson-extrapolated (h = 0) phases of the COCAL and LORENE initial data using the L, M, H resolutions. As is quite apparent, even after approximately one orbit, the evolutions resulting from COCAL and LORENE initial data differ by as much as 0.1 radians, and the difference is approximately 1.4 radians after a bit more than three orbits, thus yielding a relative difference of 3.5%. Stated differently, despite employing initial data referring to essentially the same physical binary and computed by two highly accurate numerical codes measuring global differences in mass and angular momentum that are ≤0.02%, and local differences in the whole initial-data set  $\{\alpha, \psi, K_{ii}, \rho, u^i, \Omega, C\}$  that are  $\lesssim 1\%$ , the extrapolated gravitational-wave phases at the merger time can have relative differences of ~3.5%. Considering that these results have been obtained after using rather high spatial resolutions, we believe that the use of a high-order numerical code such as WHISKYTHC has been crucial in bringing out these differences.

### V. CONCLUSIONS

We have presented the first evolutions of our newly constructed initial-data code COCAL [34] and performed an accurate study on the role that slightly different initial data play on the evolution of neutron-star binaries. The COC2CAC driver, which enables communication with existing evolution codes in the CACTUS toolkit, was presented; and a detailed convergence analysis, both with respect to the initial data itself, as well as with respect to the WHISKYTHC evolution code, was performed for the case of irrotational neutron-star binaries separated at 45 km. In addition, for benchmark purposes regarding future spinning simulations, we have also examined a corotating solution at 45 km.

Our main goals in this work have been, on the one hand, to validate the accuracy of the initial data constructed by this new initial data code, which is based on finite differences rather than spectral methods; and, on the other hand, to estimate potential differences on the gravitational-wave signal as it is produced by different initial-data codes. For this purpose, we have used the widely used, open-source code LORENE and have carried out a close comparison for the initial data computed with the codes when considering the same physical binary. For the first time, we have also explored the impact that the minute differences in the two initial-data sets have on the extrapolated gravitational-wave signal.

In this way, we have found that although the initial data between the two codes have differences in *global* quantities, such as mass and angular momentum, that are  $\lesssim 0.02\%$ , the *local* (i.e., pointwise) comparison of the initial-data quantities, such as rest-mass density, extrinsic curvature, or angular velocity, show differences of the order of  $\lesssim 1\%$ . These differences, in turn, lead to a dephasing of the extrapolated gravitational-wave signal at the merger time (after about three orbits) of approximately 1.4 radians; i.e., a relative phase error of 3.5%. Our results are a reminder of the extra care that needs to be taken when comparisons are performed between results that start from slightly different initial data, or when the initial-data errors are not properly taken into account in the simulation error budget.

### **ACKNOWLEDGMENTS**

We thank David Radice for help with WHISKYTHC and for the analysis of the gravitational waves, and Keisuke Taniguchi for clarifying issues related to the LORENE code. A. T. is supported by Vibetech Consultants. This work was supported by JSPS Grants-in-Aid for Scientific Research (C) No. 15K05085 and No. 25400262, by "NewCompStar," COST Action No. MP1304, from the LOEWE Program in HIC for FAIR, and the European Union's Horizon 2020 Research and Innovation Programme under Grant agreement No. 671698 (call

 $<sup>^8</sup>$ To compute the relative phase difference, we consider the phase difference normalized by the average total phase 39.58 = 42.33 - 2.75 radians (the latter being the average phase difference at  $t - r_{\star} = 0$ ).

FETHPC-1-2014, project ExaHyPE). The simulations were performed on SuperMUC at LRZ-Munich and on LOEWE at CSC-Frankfurt.

# APPENDIX: POINTWISE COMPARISON OF COROTATING SOLUTIONS

Although corotating solutions are not considered as physically realistic because the shear viscosity in neutron stars is too small to guarantee that this tidal coupling takes place [43,44], in this appendix we calculate a corotating neutron-star binary at 45 km and compare our solutions pointwise with a solution calculated from LORENE. The reason is that corotating binaries are easier to calculate, since the fluid rotates at the same angular velocity as the binary, and hence they can be considered as a benchmark for error estimation in binary calculations. Also, since they represent the simplest spinning-binary configuration, they provide insight for the magnitude of the error introduced by more complicated arbitrary spinning solutions.

To enforce corotation, we set  $V^{\alpha} = 0$ , and the Eulerian velocity is then given by

$$U^i = \frac{\omega^i}{\alpha}.\tag{A1}$$

We only consider the Hs3.0d resolution, and the main physical quantities for both COCAL and LORENE are reported in Table V. Note that the central rest-mass density is smaller than for the irrotational binary, while the ADM mass and angular momentum are slightly larger. This is simply due to the stellar rotation, which tends to stabilize the binary by including rotational kinetic energy.

In Fig. 10, we plot along the positive x axis the conformal factor, the lapse function  $\alpha$ , the xy component of the extrinsic curvature, the rest-mass density  $\rho$ , the y

TABLE V. Physical parameters for a corotating binary computed with either COCAL or LORENE (see Table III for a description of the various quantities). The resolution used for COCAL is Ha3.0d of Table I, except for the parameter  $r_s = 0.7925$ , in order to create a binary at separation 44.7 km.

	LORENE	COCAL
$M_0$	1.625 04	1.625 05
$M_{ m ADM}$	3.002 74	3.002 75
$M_{ m K}$		3.002 43
$\rho_c(\times 10^{-4})$	9.046 01	9.049 69
$J_{ m ADM}$	9.762 87	9.759 09
$\Omega[\text{rad/sec}]$	1857.82	1848.84
$d_s[\mathrm{km}]$	44.731	44.736
$R_{\rm eq}[{ m km}]$	14.193	14.181

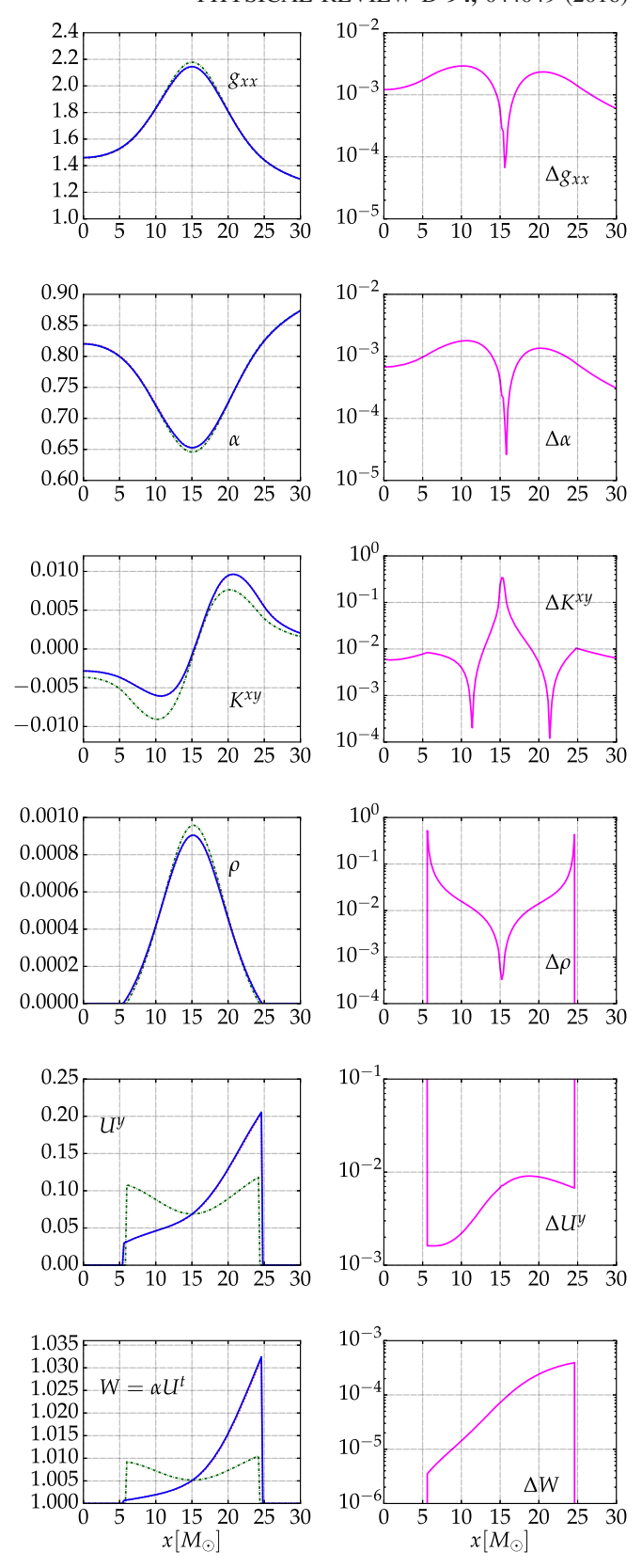
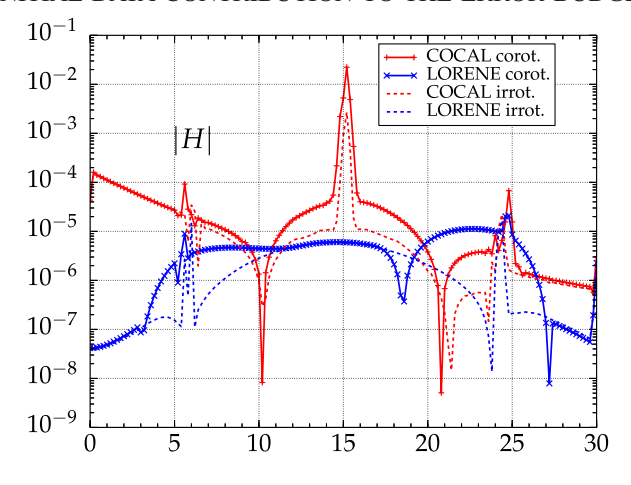


FIG. 10. The same as in Fig. 2, but for a corotating binary. The dashed green line refers to the irrotational solution in Fig. 2, which has a very similar mass (cf. Tables III and V).



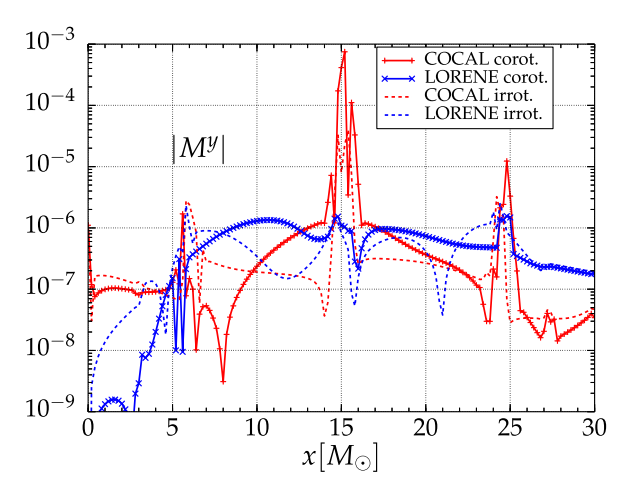


FIG. 11. Hamiltonian (top) and momentum violations (bottom) for the y component of the shift  $(\beta^y)$  along the x axis for corotating (solid lines) neutron star binaries. Dashed lines are the corresponding irrotational COCAL and LORENE violations as they appear in Fig. 4. The origin x=0 corresponds to the center of mass of the binary, with the surface of the stars located at  $x\approx 6~M_{\odot}$  and at  $x\approx 24~M_{\odot}$ . Grid parameters used in COCAL are those of Hs3.0d.

component of the velocity, and the Lorentz factor for both the COCAL (red lines) and LORENE (blue lines) solutions. As in Fig. 2, x = 0 corresponds to the center of mass of the system. Also plotted with a dashed green line is the corresponding irrotational solution as reported in Fig. 2. A rapid inspection shows that the conformal factor and the lapse are slightly smaller inside the star, while the extrinsic curvature increases (decreases) towards the outer (inner) part of the star. Also, the velocity profile has much larger values in the outer parts of the star (i.e., those farther away from the center of mass), and this is an obvious manifestation of the large spin component introduced by the corotation that is reflected in the Lorentz factor too. Overall, and as for the irrotational case, here the differences between the two data sets are also  $\leq 1\%$ .

In Fig. 11, we plot the constraint violations as we have done in Fig. 4 for the irrotational binaries. Only one resolution for COCAL, the Hs3.0d, is plotted, together with the corresponding violations from the irrotational solutions (shown with dashed lines; cf. Fig. 4), for comparison.

The comparison with the results from LORENE shows a very similar behavior to the one already discussed for the irrotational case: the Hamiltonian violations are larger, but the violations of the momentum constraint are smaller. Comparing instead the COCAL irrotational data with the corotating cases, we see that the violations are larger in the corotating binary. Hence, although the fluid formulation is significantly more complicated in the case of irrotational binaries, the large rotation present in corotating binaries induces a small amount of extra violations for both finite-difference and spectral-method codes. We expect that a similar behavior will be shown also by neutron-star binaries with arbitrary spins.

<sup>[1]</sup> B. P. Abbott *et al.* (LIGO Scientific and Virgo Collaborations), Phys. Rev. Lett. **116**, 061102 (2016).

<sup>[2]</sup> A. A. Abramovici, W. Althouse, R. P. Drever, Y. Gursel, S. Kawamura, F. Raab, D. Shoemaker, L. Sievers, R. Spero, K. S. Thorne, R. Vogt, R. Weiss, S. Whitcomb, and M. Zuker, Science 256, 325 (1992).

<sup>[3]</sup> T. Accadia *et al.*, Classical Quantum Gravity **28**, 114002 (2011).

<sup>[4]</sup> K. Kuroda (LCGT Collaboration), Classical Quantum Gravity 27, 084004 (2010).

<sup>[5]</sup> Y. Aso, Y. Michimura, K. Somiya, M. Ando, O. Miyakawa, T. Sekiguchi, D. Tatsumi, and H. Yamamoto, Phys. Rev. D 88, 043007 (2013).

<sup>[6]</sup> M. Punturo et al., Classical Quantum Gravity 27, 084007 (2010).

<sup>[7]</sup> R. Narayan, B. Paczynski, and T. Piran, Astrophys. J. Lett. 395, L83 (1992).

<sup>[8]</sup> D. Eichler, M. Livio, T. Piran, and D. N. Schramm, Nature (London) 340, 126 (1989).

<sup>[9]</sup> L. Rezzolla, B. Giacomazzo, L. Baiotti, J. Granot, C. Kouveliotou, and M. A. Aloy, Astrophys. J. Lett. 732, L6 (2011).

<sup>[10]</sup> I. Bartos, P. Brady, and S. Marka, Classical Quantum Gravity 30, 123001 (2013).

<sup>[11]</sup> E. Berger, Annu. Rev. Astron. Astrophys. **52**, 43 (2014).

- [12] J. M. Lattimer and D. N. Schramm, Astrophys. J. Lett. 192, L145 (1974).
- [13] L.-X. Li and B. Paczynski, Astrophys. J. 507, L59 (1998).
- [14] N. R. Tanvir, A. J. Levan, A. S. Fruchter, J. Hjorth, R. A. Hounsell, K. Wiersema, and R. L. Tunnicliffe, Nature (London) 500, 547 (2013).
- [15] E. Berger, W. Fong, and R. Chornock, Astrophys. J. 774, L23 (2013).
- [16] M. Tanaka and K. Hotokezaka, Astrophys. J. 775, 113 (2013).
- [17] S. Rosswog, O. Korobkin, A. Arcones, F.-K. Thielemann, and T. Piran, Mon. Not. R. Astron. Soc. 439, 744 (2014).
- [18] Y. Sekiguchi, K. Kiuchi, K. Kyutoku, and M. Shibata, Phys. Rev. D 91, 064059 (2015).
- [19] D. Radice, F. Galeazzi, J. Lippuner, L. F. Roberts, C. D. Ott, and L. Rezzolla, Mon. Not. R. Astron. Soc. 460, 3255 (2016).
- [20] B. Yang, Z.-P. Jin, X. Li, S. Covino, X.-Z. Zheng, K. Hotokezaka, Y.-Z. Fan, T. Piran, and D.-M. Wei, Nat. Commun. 6, 7323 (2015).
- [21] Z.-P. Jin, K. Hotokezaka, X. Li, M. Tanaka, P. D'Avanzo, Y.-Z. Fan, S. Covino, D.-M. Wei, and T. Piran, arXiv: 1603.07869.
- [22] M. Shibata and K. Uryū, Phys. Rev. D 61, 064001 (2000).
- [23] L. Baiotti, B. Giacomazzo, and L. Rezzolla, Phys. Rev. D 78, 084033 (2008).
- [24] Y. Sekiguchi, K. Kiuchi, K. Kyutoku, and M. Shibata, Phys. Rev. Lett. 107, 211101 (2011).
- [25] K. Takami, L. Rezzolla, and L. Baiotti, Phys. Rev. D 91, 064001 (2015).
- [26] Y. Sekiguchi, K. Kiuchi, K. Kyutoku, and M. Shibata, Phys. Rev. Lett. 107, 051102 (2011).
- [27] F. Galeazzi, W. Kastaun, L. Rezzolla, and J. A. Font, Phys. Rev. D 88, 064009 (2013).
- [28] M. Anderson, E. W. Hirschmann, L. Lehner, S. L. Liebling, P. M. Motl, D. Neilsen, C. Palenzuela, and J. E. Tohline, Phys. Rev. Lett. 100, 191101 (2008).
- [29] Y. T. Liu, S. L. Shapiro, Z. B. Etienne, and K. Taniguchi, Phys. Rev. D 78, 024012 (2008).
- [30] B. Giacomazzo, L. Rezzolla, and L. Baiotti, Mon. Not. R. Astron. Soc. 399, L164 (2009).
- [31] K. Kiuchi, K. Kyutoku, Y. Sekiguchi, M. Shibata, and T. Wada, Phys. Rev. D 90, 041502 (2014).
- [32] K. Dionysopoulou, D. Alic, and L. Rezzolla, Phys. Rev. D 92, 084064 (2015).
- [33] K. Uryū, A. Tsokaros, and P. Grandclement, Phys. Rev. D **86**, 104001 (2012).
- [34] A. Tsokaros, K. Uryū, and L. Rezzolla, Phys. Rev. D 91, 104030 (2015).
- [35] LORENE Langage Objet pour la RElativité NumériquE, http://www.lorene.obspm.fr.
- [36] P. Grandclement, J. Comput. Phys. 229, 3334 (2010).
- [37] W. Tichy, Classical Quantum Gravity 26, 175018 (2009).
- [38] W. Tichy, Phys. Rev. D 86, 064024 (2012).
- [39] SpEC Spectral Einstein Code, http://www.black-holes.org/ SpEC.html.
- [40] W. E. East, F. M. Ramazanoğlu, and F. Pretorius, Phys. Rev. D 86, 104053 (2012).
- [41] B. Brügmann, J. A. González, M. Hannam, S. Husa, U. Sperhake, and W. Tichy, Phys. Rev. D 77, 024027 (2008).

- [42] T. W. Baumgarte, G. B. Cook, M. A. Scheel, S. L. Shapiro, and S. A. Teukolsky, Phys. Rev. D 57, 7299 (1998).
- [43] C. S. Kochanek, Astrophys. J. 398, 234 (1992).
- [44] L. Bildsten and C. Cutler, Astrophys. J. 400, 175 (1992).
- [45] K. Kyutoku, M. Shibata, and K. Taniguchi, Phys. Rev. D 90, 064006 (2014).
- [46] N. Moldenhauer, C. M. Markakis, N. K. Johnson-McDaniel, W. Tichy, and B. Brügmann, Phys. Rev. D 90, 084043 (2014).
- [47] S. Bernuzzi, T. Dietrich, W. Tichy, and B. Brügmann, Phys. Rev. D **89**, 104021 (2014).
- [48] W. Kastaun, F. Galeazzi, D. Alic, L. Rezzolla, and J. A. Font, Phys. Rev. D **88**, 021501 (2013).
- [49] P. Tsatsin and P. Marronetti, Phys. Rev. D 88, 064060 (2013).
- [50] T. Dietrich, N. Moldenhauer, N. K. Johnson-McDaniel, S. Bernuzzi, C. M. Markakis, B. Brügmann, and W. Tichy, Phys. Rev. D 92, 124007 (2015).
- [51] N. Tacik, F. Foucart, H. P. Pfeiffer, R. Haas, S. Ossokine, J. Kaplan, C. Muhlberger, M. D. Duez, L. E. Kidder, M. A. Scheel, and B. Szilágyi, Phys. Rev. D 92, 124012 (2015).
- [52] K. Uryū and A. Tsokaros, Phys. Rev. D 85, 064014 (2012).
- [53] A. Tsokaros and K. Uryū, J. Eng. Math. 82, 133 (2013).
- [54] D. Radice, L. Rezzolla, and F. Galeazzi, Mon. Not. R. Astron. Soc. 437, L46 (2014).
- [55] D. Radice, L. Rezzolla, and F. Galeazzi, Classical Quantum Gravity 31, 075012 (2014).
- [56] D. Radice, L. Rezzolla, and F. Galeazzi, Numerical Modeling of Space Plasma Flows ASTRONUM-2014, Long Beach, CA, USA, June 23-27, Astronomical Society of the Pacific Conference Series Vol. 498 (2015), 121.
- [57] I. Hinder et al., Classical Quantum Gravity 31, 025012 (2013).
- [58] L. Baiotti, M. Shibata, and T. Yamamoto, Phys. Rev. D 82, 064015 (2010).
- [59] J. S. Read, L. Baiotti, J. D. E. Creighton, J. L. Friedman, B. Giacomazzo, K. Kyutoku, C. Markakis, L. Rezzolla, M. Shibata, and K. Taniguchi, Phys. Rev. D 88, 044042 (2013).
- [60] Cactus Computational Toolkit, http://www.cactuscode.org.
- [61] L. Rezzolla and O. Zanotti, *Relativistic Hydrodynamics* (Oxford University Press, Oxford, UK, 2013).
- [62] F. Löffler, J. Faber, E. Bentivegna, T. Bode, P. Diener, R. Haas, I. Hinder, B. C. Mundim, C. D. Ott, E. Schnetter, G. Allen, M. Campanelli, and P. Laguna, Classical Quantum Gravity 29, 115001 (2012).
- [63] Einstein Toolkit: Open Software for Relativistic Astrophysics, http://einsteintoolkit.org.
- [64] A. A. Tsokaros and K. Uryū, Phys. Rev. D 75, 044026 (2007).
- [65] X. Huang, C. Markakis, N. Sugiyama, and K. Uryū, Phys. Rev. D 78, 124023 (2008).
- [66] K. Uryū, A. Tsokaros, F. Galeazzi, H. Hotta, M. Sugimura, K. Taniguchi, and S. Yoshida, Phys. Rev. D 93, 044056 (2016).
- [67] K. Taniguchi and M. Shibata, Astrophys. J. Suppl. Ser. 188, 187 (2010).
- [68] F. Banyuls, J. A. Font, J. M. Ibáñez, J. M. Martí, and J. A. Miralles, Astrophys. J. 476, 221 (1997).
- [69] A. Suresh and H. T. Huynh, J. Comput. Phys. 136, 83 (1997).
- [70] D. Brown, P. Diener, O. Sarbach, E. Schnetter, and M. Tiglio, Phys. Rev. D 79, 044023 (2009).
- [71] T. Nakamura, K. Oohara, and Y. Kojima, Prog. Theor. Phys. Suppl. **90**, 1 (1987).

- [72] M. Shibata and T. Nakamura, Phys. Rev. D 52, 5428 (1995).
- [73] T. W. Baumgarte and S. L. Shapiro, Phys. Rev. D 59, 024007 (1998).
- [74] D. Alic, C. Bona-Casas, C. Bona, L. Rezzolla, and C. Palenzuela, Phys. Rev. D 85, 064040 (2012).
- [75] L. Baiotti, I. Hawke, P. J. Montero, F. Löffler, L. Rezzolla, N. Stergioulas, J. A. Font, and E. Seidel, Phys. Rev. D 71, 024035 (2005).
- [76] L. Baiotti and L. Rezzolla, Phys. Rev. Lett. 97, 141101 (2006).
- [77] L. Rezzolla and K. Takami, Phys. Rev. D **93**, 124051 (2016).
- [78] E. Schnetter, S. H. Hawley, and I. Hawke, Classical Quantum Gravity **21**, 1465 (2004).
- [79] Adaptive mesh refinement with Carpet, http://www.carpetcode.org/.